



HAL
open science

Experimental Investigation of Allotropic Transformation of Cobalt: Influence of Temperature Cycle, Mechanical Loading and Starting Microstructure

Nadjib Iskounen, Pierre-Antoine Dubos, Jamal Fajoui, Michel Coret, Marie-José Moya, Baptiste Girault, Nicolas Barrier, Nicolas Bruzy, Eric Hug, David Gloaguen

► To cite this version:

Nadjib Iskounen, Pierre-Antoine Dubos, Jamal Fajoui, Michel Coret, Marie-José Moya, et al.. Experimental Investigation of Allotropic Transformation of Cobalt: Influence of Temperature Cycle, Mechanical Loading and Starting Microstructure. Metallurgical and Materials Transactions A, 2021, 52, pp.1477-1491. 10.1007/s11661-021-06142-7. hal-03408430

HAL Id: hal-03408430

<https://hal.science/hal-03408430v1>

Submitted on 29 Oct 2021

HAL is a multi-disciplinary open access archive for the deposit and dissemination of scientific research documents, whether they are published or not. The documents may come from teaching and research institutions in France or abroad, or from public or private research centers.

L'archive ouverte pluridisciplinaire **HAL**, est destinée au dépôt et à la diffusion de documents scientifiques de niveau recherche, publiés ou non, émanant des établissements d'enseignement et de recherche français ou étrangers, des laboratoires publics ou privés.



Distributed under a Creative Commons Attribution 4.0 International License

1 **Experimental investigation of allotropic transformation of cobalt: influence of**
2 **temperature cycle, mechanical loading and starting microstructure**

3

4 Nadjib ISKOUNEN^a, Pierre-Antoine DUBOS^{a*}, Jamal FAJOU^a, Michel CORET^a,
5 Marie-José MOYA^a, Baptiste GIRAULT^a, Nicolas BARRIER^b, Nicolas BRUZY^a, Eric
6 HUG^b, David GLOAGUEN^a

7

8 ^a Université de Nantes - Centrale Nantes, Institut de Recherche en Génie Civil et
9 Mécanique (UMR CNRS 6183), 58 rue Michel Ange - BP 420, 44606 Saint-Nazaire
10 Cedex, France

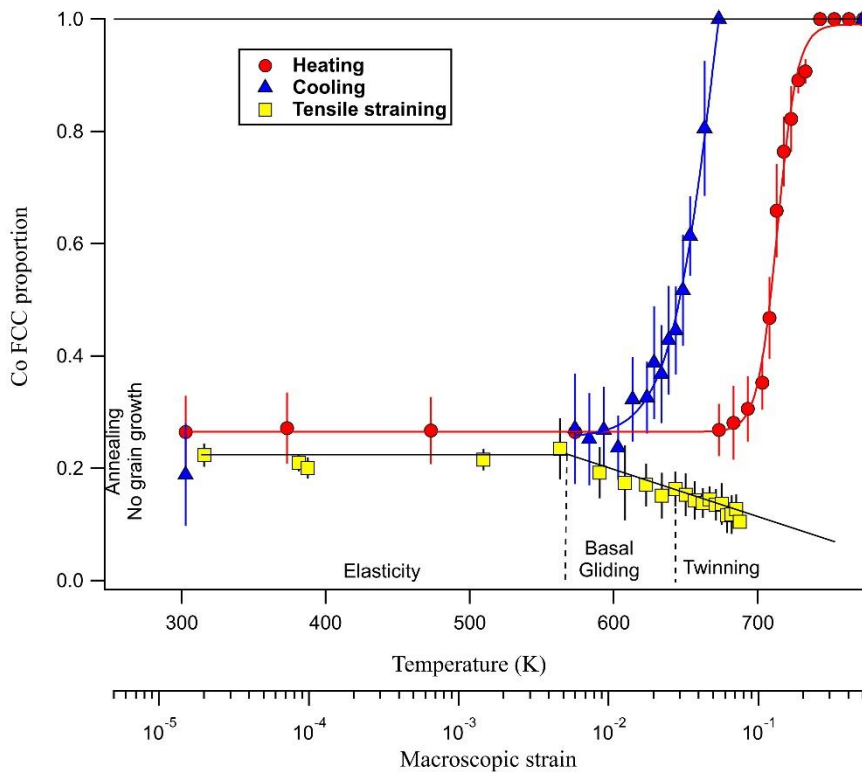
11 ^b UNICAEN, Laboratoire de Cristallographie et Sciences des Matériaux (UMR CNRS
12 6508), 6 boulevard Maréchal Juin, 14050 Caen, France

13

14 *Corresponding author: pierre-antoine.dubos@univ-nantes.fr

15

16 **Graphical abstract:** Evolution of metastable cobalt FCC volume proportion during
17 thermal cycle and mechanical loading.



18

19 **Abstract:**

20 The allotropic phase transformation in polycrystalline high-purity cobalt is incompletely
21 reversible and exhibits a temperature hysteresis. This leads to the presence of a FCC
22 metastable phase at room temperature, which alters the mechanical properties. Moreover
23 this phase transformation seems **to be able** to be induced by **the** plastic deformation. The
24 influence of thermal cycling and initial microstructure on the phase transformation has
25 been analyzed with different experimental approaches namely *in situ* X-ray diffraction,
26 differential scanning calorimetry and high temperature digital image correlation analysis.
27 A multiscale analysis, under an *in situ* tensile test, has been adopted to follow the phase
28 transformation induced by the plastic deformation. The **main** result shows that the
29 transformation is initiated by basal slip mechanisms, in competition with twinning
30 mechanisms during the second work-hardening stage.

31

32 **Keywords:**

33 Cobalt, allotropic transformation, X-ray diffraction, plastic strain, crystallographic
34 texture, *in situ* testing.

35

36 **1. Introduction**

37 Mechanical properties of metallic materials such as high-purity cobalt, are directly **link**
38 **to the** crystallographic phase structures and microstructure defects presence. The
39 mechanical behavior of two-phase cobalt remains unclear, when phase distribution and

40 evolution are not controlled. Results of the literature exhibited an important improvement
41 of the mechanical properties of cobalt when it presents a two-phase structure [1].

42 High-purity polycrystalline cobalt exhibits an allotropic transformation (reversible and
43 diffusionless) from HCP (Hexagonal Close-Packed) phase to FCC (Face Centered-Cubic)
44 on around 713 K (austenitic transformation). The reverse transformation, from FCC to
45 HCP phase (named martensitic transformation [2–4]), occurs roughly at 603 K. The
46 cobalt transformations lead to a temperature hysteresis which depends on the number of
47 applied thermal transformation cycles [4,5].

48 Most of the time, cobalt martensitic transformation remains incomplete. Consequently, a
49 residual FCC phase persists at room temperature in association with the predominant HCP
50 phase [3,6,7].

51 Sanderson [7] investigated the tensile properties of polycrystalline cobalt at room
52 temperature so as to get the HCP phase stable, using different initial retained FCC phase
53 volume proportions, grain sizes and purity samples. He found that the retained FCC phase
54 volume fraction of polycrystalline cobalt, at room temperature, depends on the thermal
55 history, the purity and the grain size. Marx *et al.* [8] studied by X-Ray Diffraction (XRD)
56 the strain-induced phase transformation, at room temperature, in a 2 μm thick film
57 deposited on polyimide substrate, using *in situ* tensile tests. They have shown that the
58 untransformed metastable FCC phase was reduced from 51 % down to 8 % when the total
59 macroscopic strain increases from 2 % up to 8 %.

60 Martinez *et al.* [9] investigated the dislocation microstructure of deformed polycrystalline
61 cobalt by analyzing the different modes responsible for plastic strain. They have observed
62 two distinct work hardening stages: a stage A, up to 4 % of plastic strain, where basal
63 dislocation glide is the main deformation mechanism, and a stage B, where plastic

64 deformation is mostly accommodated by twinning mechanisms, in agreement with Seeger
65 *et al.* [10]. These different deformation stages were also observed by Fleurier *et al.* [11].
66 HCP cold rolled metals tend to exhibit a specific deformation texture, called basal texture.
67 A principal $\{00.1\}$ basal texture component was indeed observed in polycrystalline rolled
68 cobalt by Electron Back Scatter Diffraction (EBSD) [3,9]. The phase transformation in
69 high-purity cobalt occurs by the glide of dislocations, due to the shear stress, on the habit
70 $\{111\}_{\text{FCC}}//\{00.1\}_{\text{HCP}}$ planes [12]. Hesemann *et al.* [13,14] studied the influence of the
71 texture on martensitic transformation in cobalt thin films, by varying the habit plane
72 inclination angle from film surface, at different temperatures using *in situ* synchrotron
73 XRD. They have observed that the phase transformation depends on the inclination angle
74 between $\{111\}_{\text{FCC}}//\{00.1\}_{\text{HCP}}$ planes and the film surface, this transformation arising
75 more easily at intermediary inclination of about 20° .
76 The present study focuses on the understanding of the allotropic transformation of
77 polycrystalline high-purity cobalt, which might be affected by the initial microstructure
78 as well as the thermal and mechanical loadings, using several characterization techniques.
79 After a detailed description of the experimental methods, allotropic transformation
80 behavior during thermal cycle, such as the evolution of the FCC phase volume proportion
81 using *in situ* XRD laboratory technique, is presented. Moreover, the influence of the
82 number of applied thermal cycles on the energetic parameters, carried out by Differential
83 Scanning Calorimetry (DSC), is reported. On the other hand, an overview of the effect of
84 the initial microstructure (modulated thanks to various annealing treatments) on the phase
85 transformation is given. Finally, the strain effect on the phase transformation at room
86 temperature is presented. *In situ* tensile tests under XRD have been used to study the
87 influence of the strain hardening mechanisms onto the phase transformations.

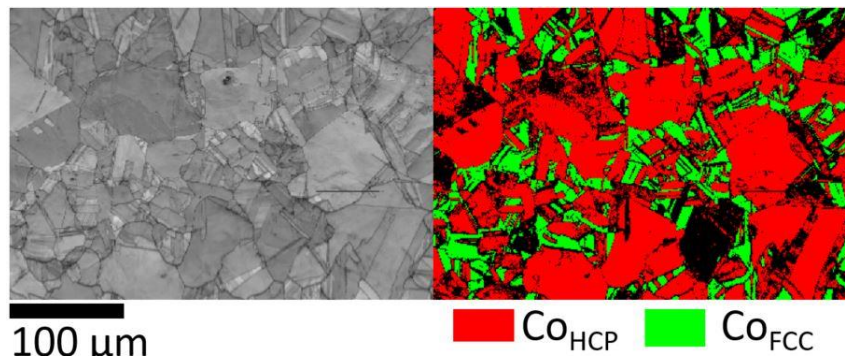
88

89 2. Material and methods

90 2.1. Characterization of as-received material

91 Commercial polycrystalline cobalt sheets (Goodfellow Company) of high-purity (99.9
92 wt. %), cold-rolled to 0.5 mm in thickness, and with a recrystallized state, were used for
93 the present study.

94 Metallographic examinations of the as-received material have revealed that the average
95 grain size is about 24 μm , with a standard deviation of 12 μm . It appears that the initial
96 microstructure displays two sets of grain shape corresponding to the two phases (HCP
97 and FCC). **Fig. 1** shows a predominant polygonal grain family population, corresponding
98 to the HCP phase, and a rather limited number of triangular and plate geometries for the
99 FCC phase.



100

101 **Figure 1:** EBSD Image Quality (IQ) map and phase cartography of as-received cobalt
102 microstructure.

103

104 Initial crystallographic textures and retained FCC phase ratio, at room temperature, were
105 determined by XRD technique. A four-circle Seifert XRD3003 PTS diffractometer

106 equipped with an Euler cradle, a Position Sensitive Detector (PSD) with a 2θ effective
107 windows of 8.6° , a 1 mm diameter collimator and an IDS camera (in order to align the
108 sample in the center of the goniometer), was used. A Cr anode ($\text{CrK}_{\alpha_{1+2}}$ radiation),
109 operating at 30 kV and 35 mA, was used (wavelength $\lambda = 2.28964 \text{ \AA}$). The K_β component
110 of the Cr radiation was eliminated using a vanadium filter installed in front of the detector.

111 Using $\theta - 2\theta$ scanning mode, the diffraction spectra were recorded from 60° to 106° in 2θ
112 with a step size of 0.05° and a counting time of 126 s/step. The analyzed reflections are
113 listed in **Table 1**. The initial averaged FCC phase volume proportion, obtained according
114 to the method described in the section 2.4.3, is about 22 %.

115 The crystallographic textures were determined from the Orientation Distribution
116 Functions (ODF) calculated by the WIMV method implemented in the BEARTEX
117 software [15], and were obtained from experimental Pole Figures (PFs) $\{10.0\}_{\text{HCP}}$,
118 $\{00.2\}_{\text{HCP}}$, $\{10.1\}_{\text{HCP}}$, $\{10.2\}_{\text{HCP}}$, $\{111\}_{\text{FCC}}$ and $\{200\}_{\text{FCC}}$ with average error coefficients
119 in the order of 0.08, except for the initial FCC phase (0.2). The declination (ψ) and
120 azimuthal (φ) angles varied from 0 to 65° ($\Delta\psi = 5^\circ$) and from 0 to 355° ($\Delta\varphi = 5^\circ$),
121 respectively. At $\varphi = 0^\circ$ and $\psi = 90^\circ$, the scattering vector was aligned with the Rolling
122 Direction (RD).

123

124 2.2. Thermal cycles and Differential Scanning Calorimetry

125 The influence of the initial microstructure (grain size and retained FCC proportion) on
126 **the** phase transformation was studied using DSC. First of all, cobalt samples were
127 annealed at a temperature set between 573 K and 1273 K for 1 h, and cooled down with

128 a cooling rate of 40 K/min. In a second step, DSC scanning was performed on four
129 samples (as-received and annealed at 573, 673 and 773 K) with a heating path up to 773 K
130 then down to 593 K (heating and cooling rate = 10 K/min) according to the methodology
131 described by Ray and Smith [2], in order to measure the HCP → FCC and FCC → HCP
132 transformation temperatures. Ray and Smith [2] showed that the austenitic transformation
133 temperature increases with higher heating rates. A phase quantification was carried out at
134 743 K with the same selected rate to ensure that the transformation was complete.

135 2.3. Macroscopic dilatometric test

136 Dilatometric tests have been performed using a homemade device on dog bone shaped
137 tensile specimens [16,17]. The samples were machined by electroerosion along the rolling
138 direction. The gage section is 5 mm in length, 5 mm in width and 0.5 mm in thickness.
139 The sample is placed into a testing box under a low pressure of Argon and heated by Joule
140 effect. A 2-color pyrometer (SensorTherm METIS M322) measures the temperature at
141 the center of the specimen starting from 300° C, due to its intrinsic emissivity. Based on
142 an alumina-based paint, a speckle pattern is deposited on the surface of the sample with
143 a fine nozzle airbrush. During the test, a high-resolution camera (Prosilica GT6600 : 6576
144 × 4384 px²) records images of a 9 × 6 mm² area. Macroscopic total strain field is then
145 computed using Digital Image Correlation method (VIC software). The images and
146 temperature values are recorded simultaneously, a dilatometric curve (total
147 strain versus temperature) can finally be obtained.

148

149 2.4. In situ X-ray diffraction measurements

150 2.4.1. Temperature

151 *In situ* experiments have been carried out in order to study the influence of the temperature
152 on the phase transformation behavior. The variation of phase (FCC and HCP) ratio during
153 heating and cooling was evaluated by XRD technique on Bruker D8 advance
154 diffractometer operating at 40 kV and 40 mA, equipped with a primary germanium (111)
155 Johansson monochromator ($\lambda_{K\alpha 1} = 1.5406 \text{ \AA}$) and a Lynxeye detector. The XRD patterns
156 were recorded in the 2θ angular range $35 - 95^\circ$ with a step size of 0.015° and a counting
157 time of 0.9 s/step. The thermal cycle (with a rate of 0.5 K/s) was conducted between 303
158 and 773 K. Despite the short counting time, the signal-to-noise ratios are only slightly
159 affected and the quality of the fitting shows, on average over all the peaks, an error of
160 0.0011° for the position and less than 5 % for the integrated intensities. The listed
161 diffraction peaks presented in **Table 1** were monitored for each temperature of the
162 thermal cycle described in **Table 2**. The temperature ranges and the heating step have
163 been chosen around the temperatures of austenitic and martensitic transformations.
164

165 **Table 1:** XRD reflections tracked for each experiment and the plane family couples used
 166 for the phase volume fraction calculations.

	Studies		
	Strain influence on phase transformation	Texture analysis	Thermal cycle influence on phase transformation
HCP plane families	{10.0}, {00.2}, {10.1} and {10.2}		{10.0}, {00.2}, {10.1}, {10.3} and {10.2}
FCC plane families	{111} and {200}		
Planes family couples	{10.0} _{HCP} /{111} _{FCC} , {10.0} _{HCP} /{200} _{FCC} , {00.2} _{HCP} /{111} _{FCC} , {00.2} _{HCP} /{200} _{FCC} , {10.1} _{HCP} /{111} _{FCC} , {10.1} _{HCP} /{200} _{FCC} , {10.1} _{HCP} /{111} _{FCC} , {10.1} _{HCP} /{200} _{FCC} , {10.2} _{HCP} /{111} _{FCC} , {10.2} _{HCP} /{200} _{FCC}		{10.0} _{HCP} /{111} _{FCC} , {10.0} _{HCP} /{200} _{FCC} , {00.2} _{HCP} /{111} _{FCC} , {00.2} _{HCP} /{200} _{FCC} , {10.1} _{HCP} /{111} _{FCC} , {10.1} _{HCP} /{200} _{FCC} , {10.3} _{HCP} /{111} _{FCC} , {10.3} _{HCP} /{200} _{FCC} , {10.2} _{HCP} /{111} _{FCC} , {10.2} _{HCP} /{200} _{FCC}

167

168

169 **Table 2:** Applied temperatures for *in situ* XRD experiments during thermal cycle
 170 (heating rate 0.5 K/s between each temperature step – 1h acquisition duration for each
 171 temperature).

	Temperature range (K)	Temperature step (K)
Initial	At 303	-
Heating	From 373 to 673	100
	From 673 to 703	10
	From 703 to 733	5
	From 733 to 773	10
Cooling	From 773 to 673	100
	From 673 to 653	10
	From 653 to 623	5
	From 623 to 573	10
Final	At 303	-

172

173 2.4.2. Tensile tests

174 *In situ* uniaxial monotonic uniaxial tensile tests were carried out, at room temperature, to
 175 study the influence of elastoplastic strain on the allotropic transformation. These
 176 mechanical tests were performed on a DEBEN device, equipped with a load cell of 5 kN
 177 capacity, and controlled by the displacement between clamping jaws. The dog bone
 178 shaped tensile specimens were machined by electroerosion with a gage section of 26 mm
 179 in length, 7 mm in width and 0.5 mm in thickness in three different directions with respect
 180 to RD: 0°/RD, 45°/RD and 90°/RD, latter corresponding thus to the Transverse Direction
 181 (TD). In the same way, as explained in 2.3, the samples were also speckled and images
 182 were recorded during the test. Digital Image Correlation have then been processed to
 183 obtain the macroscopic total strain fields.

184 The samples were strained stepwise up to 7.8 % with a strain rate of 0.2 mm/min. At each
 185 straining step, and after a stress relaxation of about 20 minutes to obtain stable mechanical
 186 fields over the entire diffracting volume, the camera images were captured and the
 187 2 θ diffraction spectra were performed with an angle ranging from 60° to 106° with a step

188 size of 0.05° and a counting time of 126 s/step. The reflections listed in **Table 1** were
189 analyzed. The crystallographic texture was also determined after the *in situ* tensile
190 experiment as described in 2.1.

191

192 2.4.3. Analysis method

193 Experimental XRD peak profiles were fitted by a Pseudo-Voigt function which takes into
194 account the $K_{\alpha 1}$ - $K_{\alpha 2}$ doublet [18]. For each diffraction peak, background was fitted
195 through a 2nd order polynomial function. Before peak profile analysis, angular corrections
196 (Lorentz, polarization and absorption factors) are also applied [19].

197 The FCC phase volume fraction (denoted f^{FCC}) has been determined for each
198 measurement point using the equation (1) as formulated by [Bonarski et al. \[20\]](#):

$$199 \quad f^{\text{FCC}} = \left(1 + \frac{I_{\text{hkl}}^{\text{HCP}} R_{\text{hkl}}^{\text{FCC}}}{I_{\text{hkl}}^{\text{FCC}} R_{\text{hkl}}^{\text{HCP}}} \right)^{-1} \quad (1)$$

200 where I_{hkl} is the integrated intensity of the corresponding $\{hkl\}$ peak. R_{hkl} is the reflectivity
201 of the lattice plane $\{hkl\}$, and is given by the following equation (2) introduced in the
202 literature [20]:

$$203 \quad R_{\text{hkl}} = \frac{1}{v^2} |F_{\text{hkl}}|^2 \left(\frac{1 + \cos^2(2\theta)}{\sin^2(2\theta)\cos(\theta)} \right) m \frac{e^{-2M}}{\mu} \quad (2)$$

204 where v is the volume of the unit cell (in Å³), F_{hkl} is the structure factor, 2θ is the
205 considered Bragg angle (in rad), m is the $\{hkl\}$ planes multiplicity factor, μ is the linear
206 absorption coefficient (in cm⁻¹) and e^{-2M} is the Debye-Waller factor [21,22].

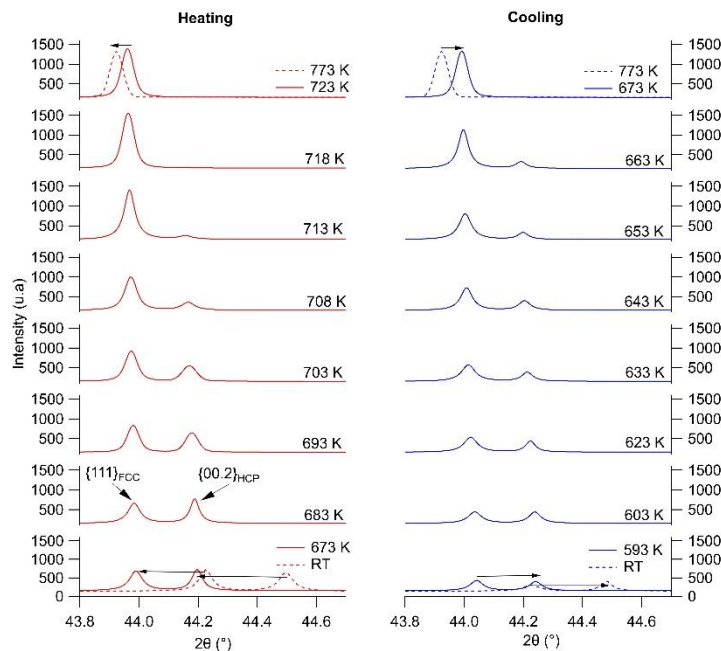
207 The volume fraction of the phases was calculated from several groups of family planes,
 208 as presented in **Table1**, to obtain the average FCC phase distribution and evaluate the
 209 influence of the texture on the quantitative phase analysis.

210 3. Results and discussion

211 3.1. Allotropic transformation characterization during thermal cycle

212 3.1.1. Phase proportion evolution and typical temperatures

213 In order to characterize the HCP \leftrightarrow FCC transformation behavior, the evolution of the
 214 integrated diffraction peak intensity for each reflection corresponding to the HCP and
 215 FCC phases were recorded as a function of the temperature. An example is given in **Fig.**
 216 **2** for $\{111\}_{\text{FCC}}$ and $\{00.2\}_{\text{HCP}}$ reflections during heating and cooling. The volume fraction
 217 of the phases can be determined according to the equations (1) and (2).

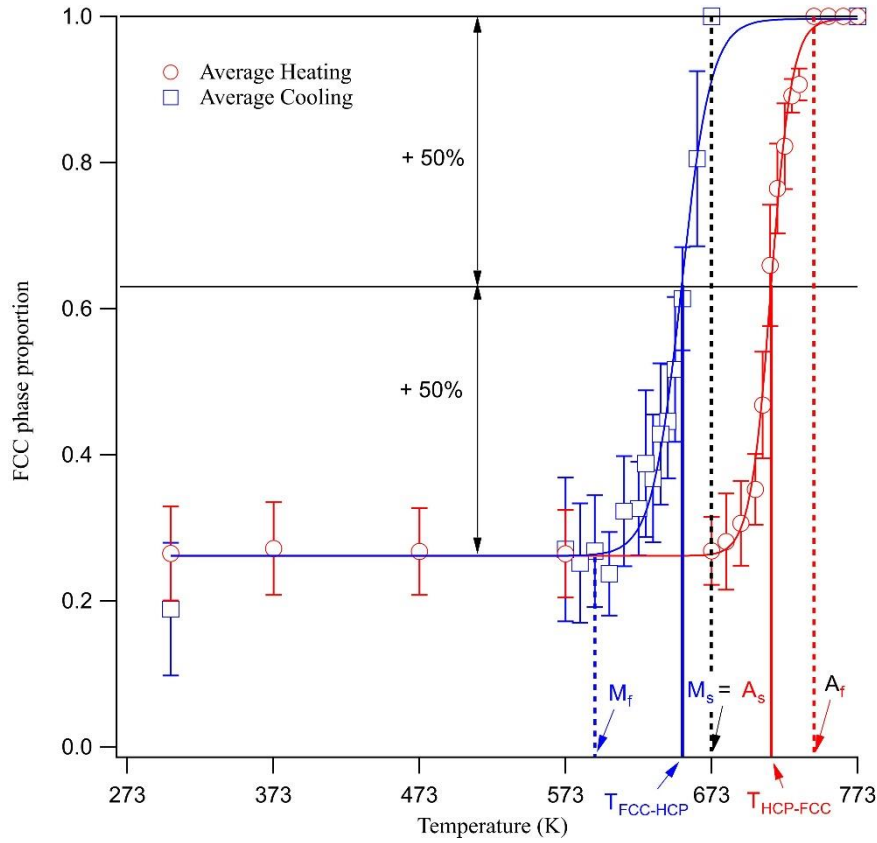


218

219 **Figure 2:** Diffraction patterns for $\{111\}_{\text{FCC}}$ and $\{00.2\}_{\text{HCP}}$ reflections during heating and
 220 cooling.

221

222 **Fig. 3** gives FCC phase proportion evolution during the thermal cycle described in
223 **Table 2**. During heating, the HCP \rightarrow FCC transformation begins at the austenitic start
224 temperature denoted $A_s = 673$ K and ends at the austenitic finish temperature named
225 $A_f = 743$ K. During cooling, the reverse transformation FCC \rightarrow HCP arises at the
226 martensitic start temperature $M_s = 673$ K and comes back to its original state when the
227 martensitic finish temperature of $M_f = 593$ K is reached. The two experimental curves
228 can be fitted by sigmoidal laws which allow to define the transformation temperatures
229 $T_{HCP-FCC}$ and $T_{FCC-HCP}$. These temperatures are determined when the FCC proportion has
230 a relative variation of 50 % over the temperature cycle, knowing that the initial proportion
231 is 26 % and that the transformation is complete during heating. With this methodology,
232 $T_{HCP-FCC} = 714$ K and $T_{FCC-HCP} = 653$ K are obtained, revealing a temperature hysteresis
233 around 60 K. One can notice that the diffraction patterns have also enabled to identify
234 CoO and Co₃O₄ oxides formation from 673 K that persist when cooling down to room
235 temperature. It is important to point out that the presence of a thin oxide layer does not
236 affect the quantification of the HCP and FCC phase proportions. Finally, it seems that the
237 phase transformation is faster during heating than during cooling. This can be related to
238 the phase transformation mechanism which is based on dislocation movements [23],
239 themselves favored by an increase in temperature.



240

241 **Figure 3:** Volume fraction of FCC phase during heating (red circle) and cooling (blue
 242 square) of cobalt calculated from XRD data. Error bars are the standard deviation on the
 243 8 couples of family planes.

244

245 3.1.2. Lattice strain measurements during the thermal cycle

246 Lattice strain of each {hkl} plane family can be determined considering lattice spacing

247 (d_{hkl}) as an elastic strain gage using the following equation [24]:

$$248 \quad \langle \varepsilon(hkl) \rangle_{V_d} = \ln \left(\frac{\langle d^{hkl} \rangle_{V_d}}{d_0^{hkl}} \right) = \ln \left(\frac{\sin \theta_0(hkl)}{\langle \sin \theta(hkl) \rangle_{V_d}} \right) \quad (3)$$

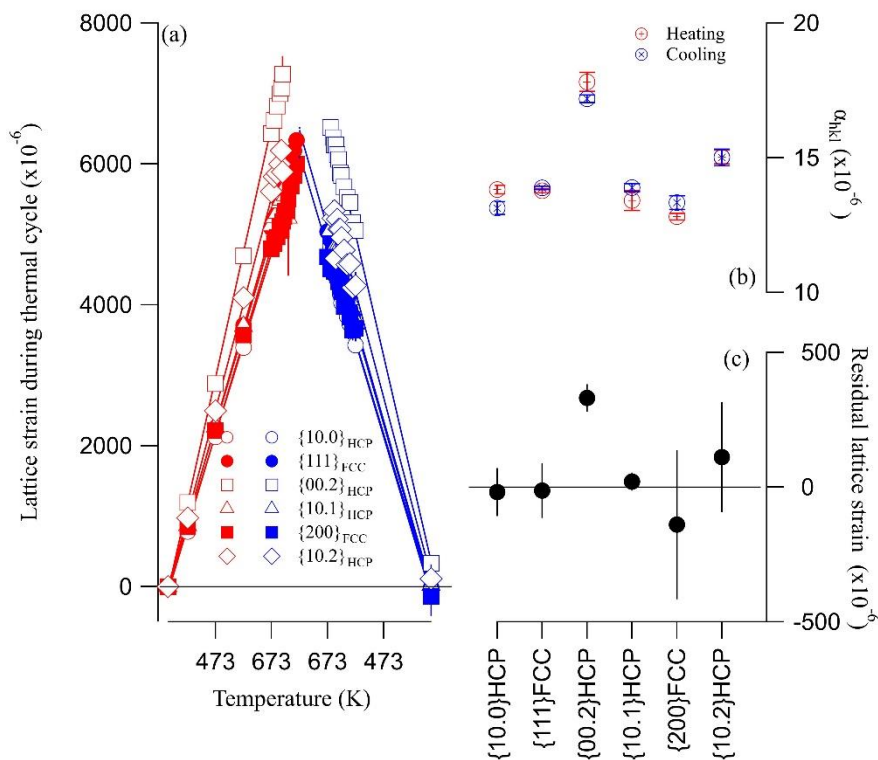
249 $\langle \varepsilon(hkl) \rangle_{V_d}$ is the elastic lattice strain. $\langle \rangle_{V_d}$ indicates an averaging over diffracting grains

250 for the considered {hkl} reflection. For a given {hkl} reflection, d_0^{hkl} and $\theta_0(hkl)$ are the

251 interplanar spacing and the diffraction angle (Bragg angle), respectively, in the

252 undeformed sample i.e. prior to any thermal or mechanical loading. **Fig. 4(a)** gives the
253 evolution of the lattice strains observed for different $\{hkl\}$ reflection of the two phases
254 during the applied thermal cycle. This evolution is linear for both heating and cooling,
255 enabling to estimate the Coefficients of Thermal Expansion (CTE) α_{hkl} for each plane
256 family within the analyzed polycrystal. The obtained values are represented in **Fig. 4(b)**
257 and are in agreement with the literature [21]. Matsumoto [4] has also shown that the CTE
258 of HCP single crystal is substantially affected by the orientation of the c -axis within the
259 sample coordinate system. Thermal cycle induces a large strain, the largest one actually
260 reaches more than 8000 μ -strain ($\times 10^{-6}$ mm/mm) for the $\{00.2\}_{\text{HCP}}$ set of grains. The
261 main thermal dilatation occurs then along the $[00.2]_{\text{HCP}}$ direction. During cooling, plastic
262 deformations are induced and can be explained by the presence of residual lattice strains.
263 These results agree with prior investigations on high-purity cobalt showing **slipping** lines
264 due to plastic deformation during the thermal cycle [23,25].

265 **Fig. 4(c)** shows the residual lattice strains present after the thermal cycle for each
266 analyzed reflection. Initially, residual strains can be considered negligible due to the
267 annealed character of the as-received materials. This allows **considering** the initial state
268 of samples as a strain-free reference. After the thermal cycle, residual lattice strains have
269 slightly increased, especially for $\{00.2\}_{\text{HCP}}$, $\{10.2\}_{\text{HCP}}$ and $\{200\}_{\text{FCC}}$ reflections.
270 Regarding uncertainties, only $\{00.2\}_{\text{HCP}}$ planes present an unambiguous residual strain of
271 a few hundred of μ -strains in tension. As shown in **Fig. 4**, these residual strains **measured**
272 after a thermal cycle are related to **the** phase transformation and its associated volume
273 variation as well as the accommodation related to the thermal and plastic anisotropies.



274

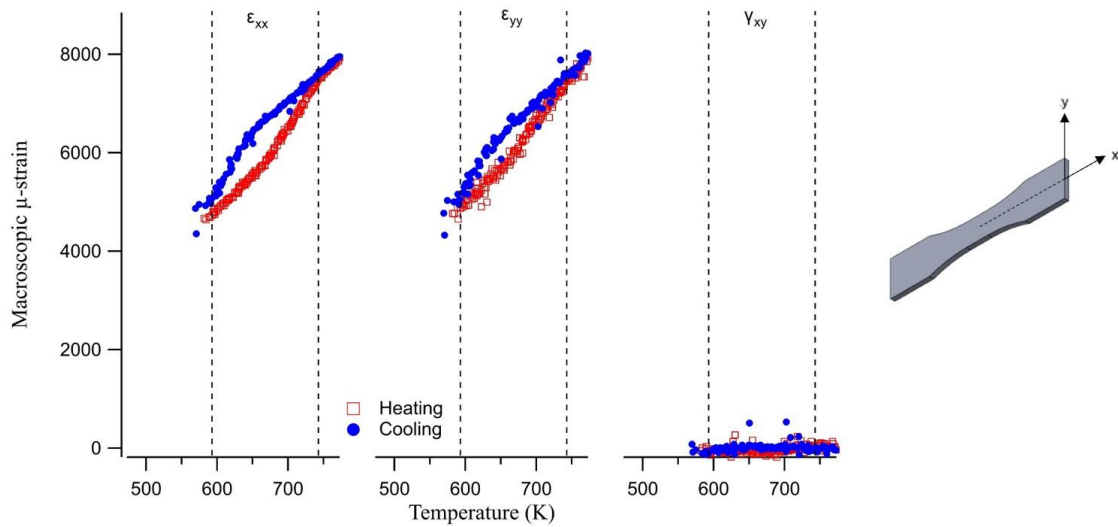
275 **Figure 4:** Mechanical state during thermal cycle considering the different tracked plane
 276 families. (a) Lattice strain evolution during heating (red) and cooling (blue). (b) Thermal
 277 expansion coefficients during heating (red open circle) and cooling (blue open circle)
 278 obtained from XRD results. (c) Measured residual lattice strains after (black solid circle)
 279 the thermal cycle.

280

281 3.1.3. Macroscopic thermal dilatation

282 The post-treatment of image correlation results enables to access to ϵ_{xx} (parallel to RD),
 283 ϵ_{yy} (parallel to the transverse direction (TD)) and γ_{xy} strain components. **Fig. 5** shows the
 284 dilatometric curves obtained by coupling the temperatures measured by pyrometer (at the
 285 center of the sample) and the strain fields obtained by image correlation method. The
 286 phase transformation induces a change of volume, due to the change of the lattice
 287 structures, of about 0.3 % in the case of high-purity polycrystalline cobalt, as reported in
 288 the literature [12,25,26]. Hence, in the temperature range between 573 K and 773 K, the

289 dilatometric curve is the consequence of the competition between thermal expansion and
290 volumetric change. As it can be seen, both dilatometric curves along x and y display a
291 temperature hysteresis caused by the phase transformation, which is not observed on the
292 lattice strains during the thermal cycle (see **Fig. 4(a)**). The difference in the scale of
293 analysis may be the reason for these observations. XRD results exhibit the combination
294 of macroscopic (or Type-I) and intergranular strains (or Type-II) whereas dilatometry
295 only gives access to macroscopic strains. The hysteresis of ϵ_{xx} dilatometric curve is
296 qualitatively slightly broader than the one of ϵ_{yy} dilatometric curve and could be explained
297 by a slight anisotropy or texture effect. Moreover, hysteresis occurs systematically
298 between the temperatures $M_f = 593$ K and $A_f = 743$ K. Beyond austenitic finish
299 temperature, A_f , the dilatometric curve displays a linear evolution (for both of ϵ_{xx} and ϵ_{yy})
300 with temperature that matches a pure thermal expansion or contraction during heating or
301 cooling, respectively. ϵ_{xx} and ϵ_{yy} strain components exhibit a quasi equibiaxial strain state
302 with an order of magnitude similar to the measured lattice strains induced by the thermal
303 cycle (see **Fig. 4**). Finally, the dilatometric curve of γ_{xy} clearly highlights the absence of
304 macroscopic planar shearing during the thermal cycle.



305

306 **Figure 5:** Dilatometric curves according to ϵ_{xx} , ϵ_{yy} and γ_{xy} during the thermal cycle. (x
307 corresponds for this experiment to the rolling direction).

308

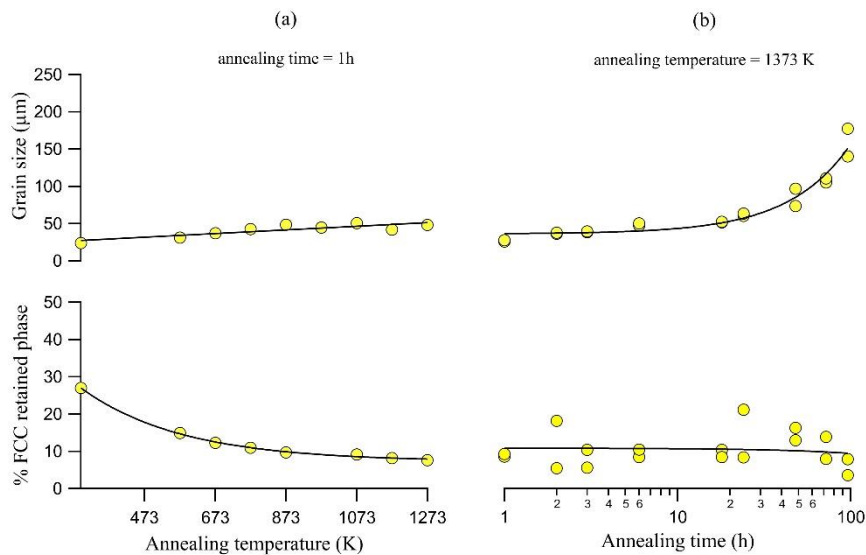
309 3.1.4. Influence of initial microstructure on the allotropic transformation

310 **Fig. 6** shows the influence of annealing temperature on the grain size and on the volume
311 fraction of the retained FCC phase. In the present work, an annealing duration of one hour
312 has been chosen in order to have a limited granular growth so that grain size evolution
313 remains a minor contribution to the microstructure changes no matter the selected
314 annealing temperature. These results are then compared with previous works for a 1373 K
315 annealing temperature with durations ranging from 1 to 96 hours [27]. The grain size,
316 deduced from metallographic observations, slightly increases with annealing temperature
317 but does not seem very significant as compared to the power type increase appearing from
318 20 hours of heat treatment at 1373 K. Concerning the proportion of retained FCC phase,
319 it exponentially decreases from 28 % (as-received) down to almost 10 % for 873 K
320 annealing, in accordance with Sanderson [7]. For annealing temperatures greater than
321 873 K or longer annealing durations, this proportion remains constant.

322 Overall, these results allow to explain the final FCC phase proportion met after the
323 thermal cycle. In fact, the thermal cycle applied during the previous *in situ* analysis was
324 including a heating stage until 773 K. This treatment has induced a complete
325 transformation of the HCP phase and significantly reduced the proportion of residual FCC
326 phase at room temperature.

327 The results of Fig. 6 clearly show that annealing treatments at moderate temperature
328 ($T_{annealing} < T_{HCP-FCC}$) enable to homogenize the microstructure with a reduction of the
329 retained FCC proportion combined with a limited grain growth. The energy required for
330 phase transformation is much lower than the one for grain growth, showing to some extent
331 the independence of these two phenomena.

332

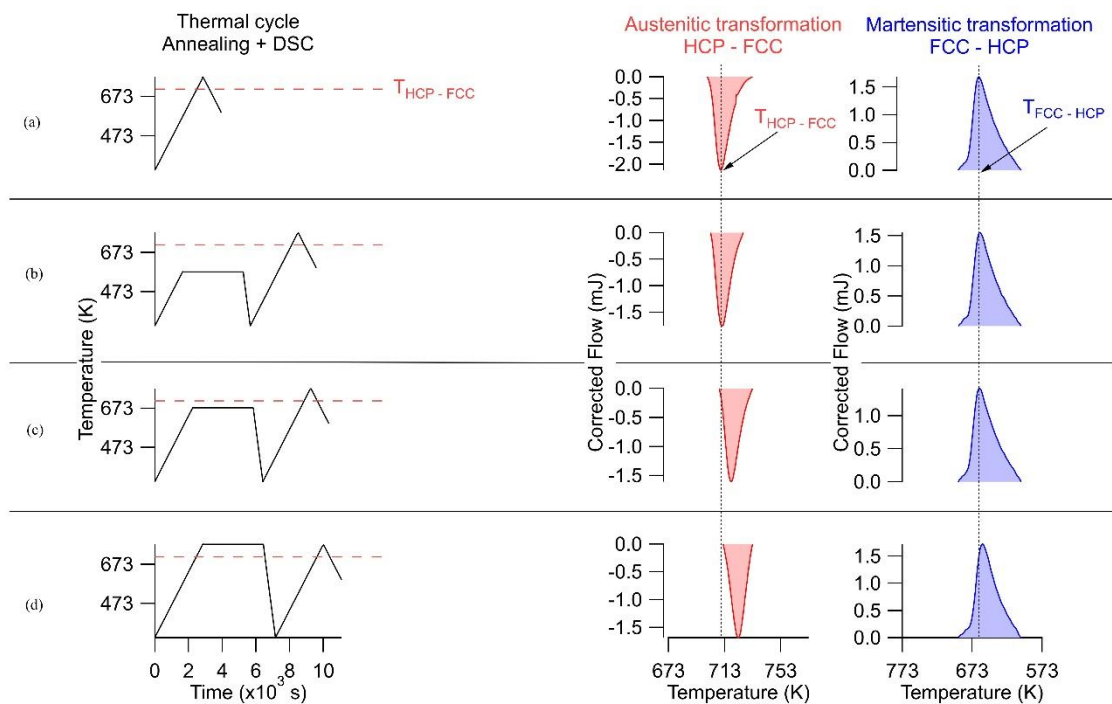


333

334 **Figure 6:** Influence of annealing conditions (temperature for a time of 1h (a) and time for
335 a temperature of 1373°K (b)) on grain size and retained FCC phase proportion evolution.

336

337 The influence of initial microstructure (i.e. retained FCC phase ratio and grain size to a
 338 lesser extent) on the phase transformation, performed using DSC, is plotted in **Fig. 7**.
 339 Austenitic and martensitic transformation peaks are tracked during the DSC thermal
 340 cycle, on the as-received Co specimen as well as on the 573 K, 673 K and 773 K annealed
 341 samples with 40 K/min cooling rate. The temperature of the HCP → FCC transformation
 342 increases with annealing temperature. The results show that the temperature to initially
 343 transform the HCP phase is directly related to the initial proportion of the retained FCC
 344 phase: the higher the annealing temperature, the lower the retained FCC volume fraction
 345 and the higher the HCP → FCC phase transformation temperature. Indeed, austenitic
 346 transformation needs more thermal energy to enable phase transformation as HCP volume
 347 fraction to be transformed increases. In return, since the reverse transformation (i.e., FCC
 348 → HCP) takes place during cooling with 100 % FCC phase (austenitic transformation is
 349 completely finished at 773 K), the martensitic transformation temperature is then
 350 unchanged during cooling.

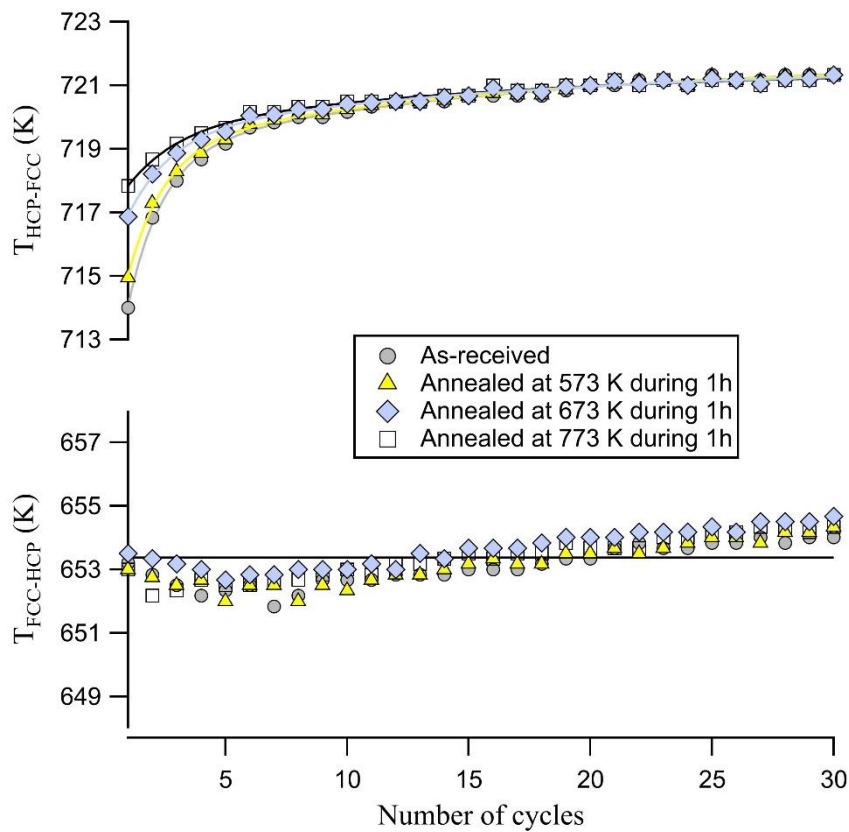


351

352 **Figure 7:** Thermal loading paths in DSC performed for as-received (a), 573 K (b), 673 K
353 (c) and 773 K (d) annealed samples with corresponding austenitic (red) and martensitic
354 (blue) transformation peak tracking.

355

356 Despite a microstructure that appears to be stable, when subjected to thermal cycles
357 around the transformation hysteresis (593 K – 773 K), the sample annealed at 773 K
358 during one hour shows (see **Fig. 8**) an austenitic temperature which only becomes stable
359 after about 15 cycles. It could be noted that the austenitization temperatures of the as-
360 received sample and the two other annealed samples stabilize at the same value (≈ 721 K).
361 This observation shows that it is necessary to transform the material about fifteen times
362 in order to homogenize it and to make its temperature $T_{HCP-FCC}$ independent of the
363 following heat treatments. As displayed in **Fig. 8**, the martensitic transformation
364 temperature does not depend on the initial microstructure and therefore on annealing
365 temperature. This is convenient with the fact that it transforms the same FCC phase
366 proportion (*i.e.* 100 %). In the same way, this transformation is insensitive to the number
367 of thermal cycles as the $T_{FCC-HCP}$ temperature varies less than 2 K.



368

369 **Figure 8:** Temperatures of HCP \rightarrow FCC and FCC \rightarrow HCP transformations as a function
 370 of the number of applied DSC cycles (up to 30 cycles) of as-received sample superposed
 371 with the result of 573 K, 673 K and 773 K annealed samples.

372 Bauer *et al.* [23] showed a grain growth of 15 to 80 μm with 60 DSC cycles, which does
 373 not influence the stabilized transformation temperature after 15 cycles. An additional
 374 study was carried out on samples with different grain sizes and the same FCC proportion
 375 ($d = 100 \mu\text{m}$, $f_{\text{FCC}} = 0.1$ for an annealed sample during 48 hours at 1373 K and $d = 25 \mu\text{m}$
 376 $f_{\text{FCC}} = 0.1$ for an annealed sample during 1 hour at 1373 K). The stabilized transformation
 377 temperature after 30 cycles is clearly independent of the initial grain size.

378 3.2. Allotropic transformation during mechanical deformation

379 3.2.1. Phase proportion evolution and work-hardening during tensile test

380 The mechanical behavior in tension can be divided in three distinct stages. The first one
381 is the elastic part. Zhou *et al.* [28,29] have shown that this stage is characterized by a
382 kinking nonlinear elasticity resulting in fully reversible hysteresis induced by nucleated
383 dislocation loops in the slipping favored plane (the basal plane in the present case).

384 The second one, named stage A, characterizes the first work-hardening stage and appears
385 from a strain of 0.0045 up to 0.018 (**Fig. 9**). This stage is associated with a large reduction
386 of the work-hardening rate and is controlled by planar and single glide of basal
387 dislocations [9]. However the combination of basal slip and volume change during
388 transformation [26] does not satisfy von Mises criterion which requires, for a polycrystal,
389 five independent shear systems to undergo homogeneous strain without changes in
390 volume. In order to accommodate the plastic deformation and since the FCC to HCP
391 phase transformation is a low energy transformation requiring only simple shear, the
392 formation of martensitic phase can be considered as equivalent to the formation of twins.

393 Above a strain level of 0.018, the slope of the work-hardening rate is lowered to an almost
394 constant value corresponding to stage B. This stage is described by twinning nucleation
395 and growth. Martinez *et al.* have shown that compression $\{10.1\}_{\text{HCP}}$ and tensile $\{10.2\}_{\text{HCP}}$
396 twins are the main twinning modes representing respectively 16 % and 66 % of total
397 observed twin planes [9].

398 **Fig. 9** highlights the effect of these deformation mechanisms on the allotropic
399 transformation, for tensile sample strained along the rolling direction. The fast track FCC
400 phase proportion, determined from $\theta - 2\theta$ spectra achieved at ($\psi = 0^\circ$, $\phi = 0^\circ$), is plotted
401 (open triangles) versus the macroscopic applied true strain. This figure shows a
402 transformation of the initial residual FCC phase into HCP phase initiated by plasticity.

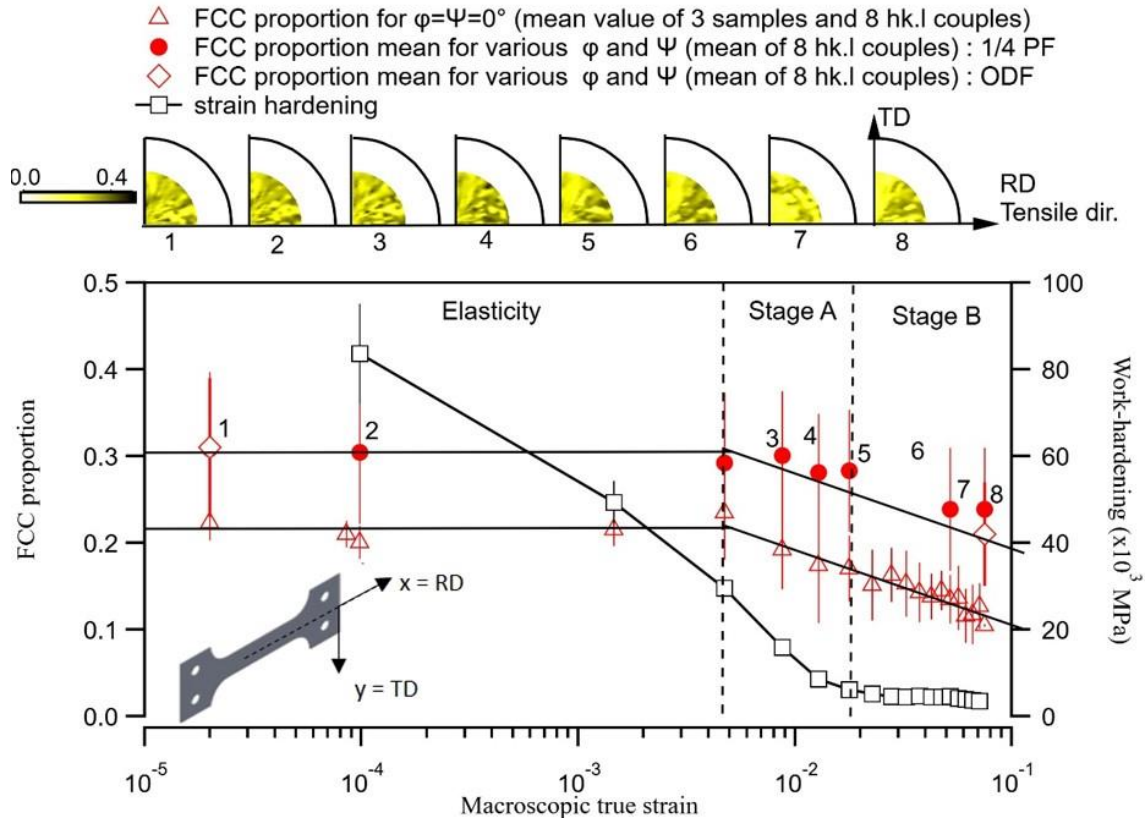
403 From the beginning of stage A to the end of stage B, this transformation is done gradually
404 and linearly with the logarithm of the applied strain. In order to ensure reliability and
405 reproducibility of the experimental data, the tests were repeated three times by three
406 different investigators. The FCC phase proportion evolution during tensile loading can be
407 expressed by the following proposed straightforward equation:

$$408 \text{ FCC proportion} = a * \log(\epsilon) + b, \quad (4)$$

409 where coefficients are $a = -0.089 \pm 0.006$, and $b = 0.017 \pm 0.01$, with a linear regression
410 coefficient $R^2 = 0.93$. In comparison, Sanderson found $a = -0.1$ and $b = 0.019$ for
411 polycrystalline samples with 10 μm grain size [6]. The experimental slope is similar in
412 stage A and in stage B, leading to the conclusion that the phase transformation does not
413 seem to be affected by the activation of twinning during stage B.

414 In order to take into account a doubtless evolution of the texture with the mechanical
415 loading and to study the anisotropy of the phase transformation, FCC phase proportion is
416 determined for each of the (ψ, φ) couples covering a quarter of a pole figure ($0^\circ < \psi <$
417 $55^\circ, 0^\circ < \varphi < 90^\circ$) using the 8 plane family couples detailed in **Table 1**. Values are then
418 averaged and results are plotted (red solid circles named $\frac{1}{4}$ PF) in **Fig 9**. Phase ratio
419 evolution shows the same tendency as the one determined at $(\psi = 0^\circ, \varphi = 0^\circ)$ for the two
420 plasticity stages, with the same slope but a b - coefficient equal to 0.117 ± 0.007 . However,
421 these averaged values are higher due to the influence of the texture on the phase
422 proportion quantitative determination. Calculations of the phase proportion [taking](#) into
423 account the ODF (red open **lozenges** in **Fig. 9**) from complete recalculated PFs have been
424 performed on the as-received material and on a specimen strained at 0.078 in order to
425 confirm the relevance of the results obtained over a quarter of experimental PF under

426 loading. As regard to the experimental complexity to carry out ODF and since the texture
 427 does not fundamentally change the results, the choice is made to simplify the
 428 quantification of phase proportions at a single position (i.e. $\psi = 0^\circ$, $\phi = 0^\circ$).



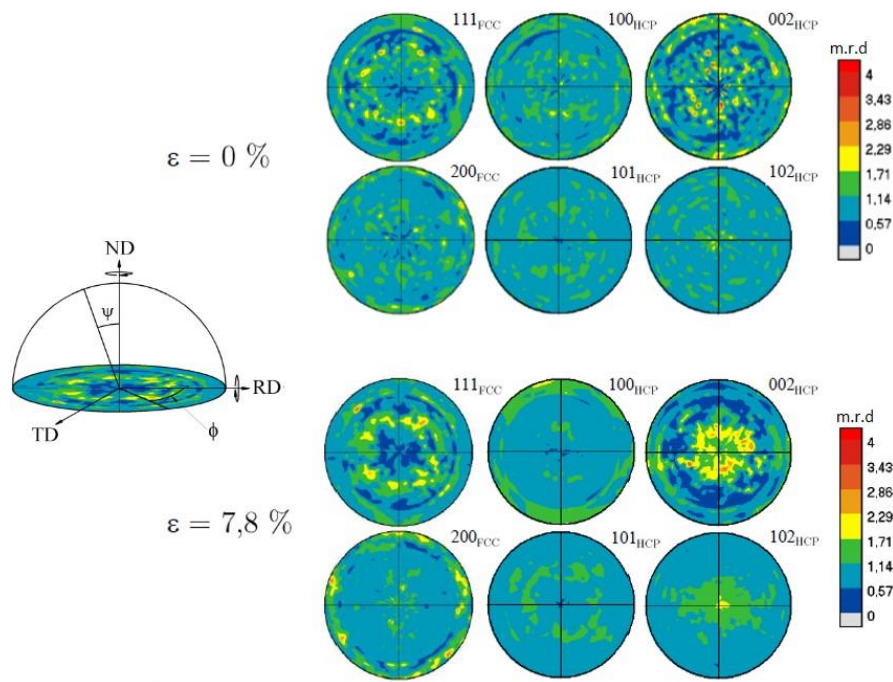
429
 430 **Figure 9:** FCC \rightarrow HCP transformation evolution as macroscopic strain increases.
 431 Relationship between FCC phase proportion (red open triangle) and the deformation
 432 stages illustrated by work-hardening (black open square). Monitoring of the phase
 433 transformation anisotropy for various (ϕ , ψ) orientations (maps) during tensile straining
 434 with the corresponding average values (red solid circle).

435

436 3.2.2. Crystallographic analysis of the strain-induced phase transformation and the
 437 deformation mechanisms.

438 Deformation mechanisms and phase transformations can be explained by a
 439 crystallographic analysis, comparing the different texture components observed on the

440 recalculated PFs obtained thanks to XRD on a sample before and after straining. **Fig. 10**
 441 shows $\{10.0\}_{\text{HCP}}$, $\{00.2\}_{\text{HCP}}$, $\{10.1\}_{\text{HCP}}$, $\{10.2\}_{\text{HCP}}$, $\{111\}_{\text{FCC}}$ and $\{200\}_{\text{FCC}}$ recalculated
 442 PFs of the as-received sample and of a sample strained at 7.8 % along RD. Except for the
 443 habit plane between HCP and the retained FCC, it can be assumed that the initial state of
 444 the HCP phase is not textured as compared to the deformed state that exhibits distinctive
 445 poles which can be seen on the majority of PFs [30].



446

447 **Figure 10:** $\{10.0\}_{\text{HCP}}$, $\{00.2\}_{\text{HCP}}$, $\{10.1\}_{\text{HCP}}$, $\{10.2\}_{\text{HCP}}$, $\{111\}_{\text{FCC}}$ and $\{200\}_{\text{FCC}}$
 448 recalculated PFs of the as-received sample and of a sample strained at 7.8 % along RD.

449

450 If the sample shows an isotropic orientation distribution in the initial state, three specific
 451 orientation cases of the HCP lattice with respect to the loading direction are assumed to
 452 be sufficient to study the orientation dependence of deformation mechanisms and phase
 453 transformation: *c-axis* parallel, normal or inclined with respect to the loading direction,
 454 as shown in **Table 3**.

455 **Table 3:** {00.2} and {10.0} PF reorientations peculiar to twinning systems and phase
 456 transformation according to the 3 studied configurations.

	Twinning system [31]	Twinning shear [32–34]	ψ-angle reorientation on {00.2} PF	ψ-angle reorientation on {10.0} PF
(a) Tension twin $\sigma//c$ -axis	{10.2} < 10.1 >	0.13	5°	85°
(b) Compression twin $\sigma \perp c$ -axis	{10.1} < 10.2 >	0.14	56°	34°
(c) FCC-HCP transformation $\sigma//(10.2)$			43° (111) 66° (11 $\bar{1}$)	

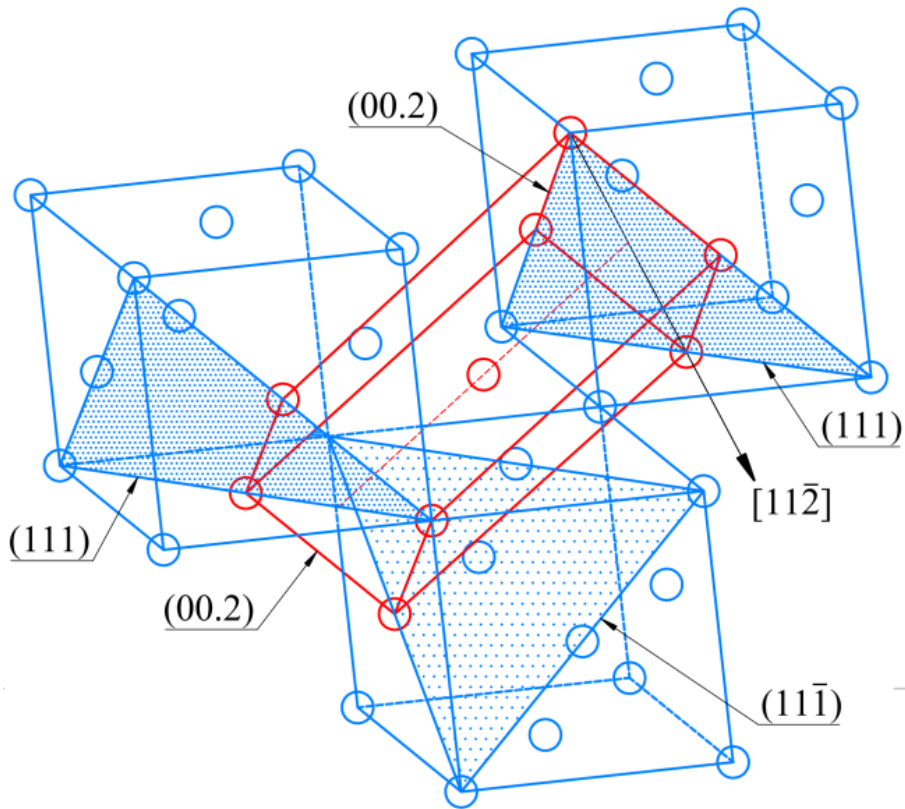
457

458 As described in the 3.2.1 subsection, the plastic behavior of high-purity polycrystalline
 459 cobalt exhibits two distinctive stages which correspond to the activity of basal slip (stage
 460 A) and twinning deformation modes (stage B). The determination of Schmid's factor of
 461 the basal plane for the three specific orientation cases ($\sigma//c$ -axis (a), $\sigma \perp c$ -axis (b) and
 462 $\sigma//(10.2)$ (c)) shows that the unique configuration enabling such a slipping activity is (c):
 463 (10.2) plane parallel to the specimen surface with a Schmid's factor close to 0.5 (most
 464 suitable configuration for basal slip). Configurations (a) and (b) will then be the most
 465 likely to show twin activity. Two types of twins have been frequently observed in
 466 deformed high-purity polycrystalline cobalt [9,33]. The first one is the tensile twin
 467 {10.2}<10.1>, which activates when the HCP lattice undergoes a tensile strain along the
 468 c -axis, because of the ratio $c/a < \sqrt{3}$ [32]. It represents 66% of the observed **twinning**
 469 modes in deformed cobalt and leads to a crystal rotation of 85°. The second one is the

470 compression twin $\{10.1\}\langle 10.2\rangle$, observed at a level of 16% and associated with a crystal
471 rotation of 56° .

472 In addition to the deformation mechanisms, strained cobalt **also presents also** a phase
473 transformation FCC \rightarrow HCP, which is diffusionless and occurs by dislocation gliding on
474 the habit plane $\{111\}\{\{00.2\}$, causing shear along the $[11\bar{2}]_{\text{FCC}}$ direction (equivalent to
475 the HCP direction $[11.0]$). The phase transformation is called multi-variant due to its
476 capability to occur on several $\{111\}_{\text{FCC}}$ planes, which display rotation angles of 70.53°
477 between them [12] (illustrated in **Fig. 11**). However, due to the compactness difference
478 between the two phases, the resulting rotational angle after the phase transformation FCC
479 \rightarrow HCP becomes 71.4° according to the orientation relationship established by Shoji-
480 Nishiyama [35]. Hence, the resulting crystal undergoes a theoretical volume change of
481 about -0.3 %, which corresponds to a slight contraction along the *c-axis* [26,36]. This
482 phase transformation is more likely to be initiated when the habit plane $\{111\}\{\{00.2\}$
483 shows an intermediary inclination as regard to the loading direction [13,14]
484 corresponding to (c) configuration in **Table 3**. The crystallographic mechanism of FCC
485 \rightarrow HCP phase transformation is illustrated in **Fig. 11**, showing the FCC lattice atoms
486 displacement along the $[11\bar{2}]$ direction and the formation of the HCP lattice from three
487 $\{111\}$ FCC planes.

488



489

490 **Figure 11:** Schematic representation of the orientation relationship between the FCC
 491 structure (in blue) and the HCP structure (in red) once shear has been achieved along the
 492 $[11\bar{2}]$ FCC direction.

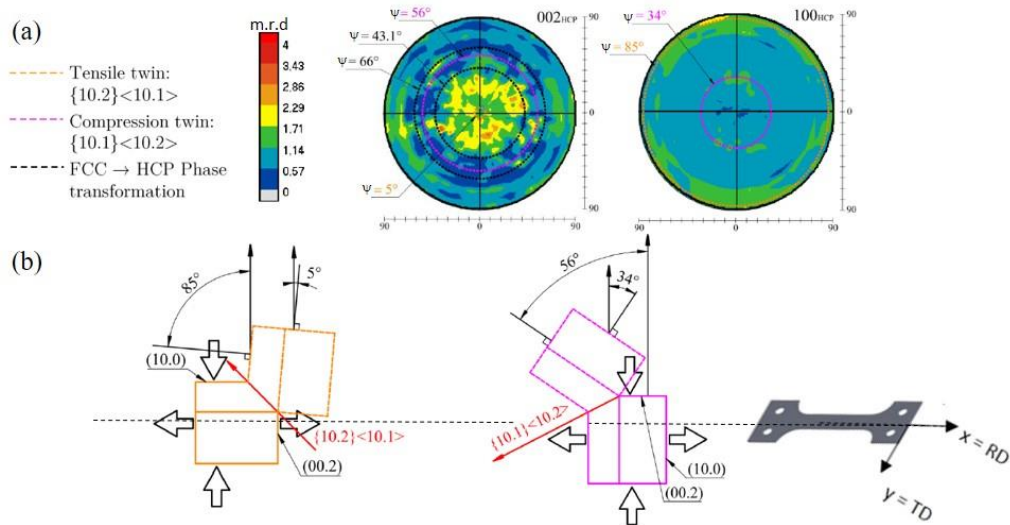
493

494 The crystallographic analysis carried out on the PFs of the deformed sample highlights
 495 the activated twin modes as well as the FCC \rightarrow HCP phase transformation induced by
 496 mechanical loading. It should be underlined that only two twin systems ($\{10.2\}\langle 10.1\rangle$
 497 for configuration (a) and $\{10.1\}\langle 10.2\rangle$ for configuration (b)) have been clearly identified
 498 using the PFs of the sample loaded up to 7.8 % strain. Those actually match the lowest
 499 shear twinning values [32–34].

500 In the first configuration considered (a), the tensile twin mode $\{10.2\}\langle 10.1\rangle$ induces a
 501 crystal reorientation of 85° . This configuration concerns the reorientation of 85° of the *c*-
 502 *axis*, which were initially parallel to the loading direction (displayed by the orange solid

503 line lattice projection in **Fig. 12 b**) and become misaligned by 5° as compared to the
504 normal of the sheet plane (ND) (displayed by orange dashed line lattice projection in **Fig.**
505 **12 b**). For the twinned part, it results in an angle of 85° between ND and the normal of
506 the twinned prismatic plane (10.0) and an angle of 5° between ND and the normal of the
507 twinned basal plane (00.2). These crystallographic reorientations of the twinned region
508 as compared to the parent crystal is depicted by intensity reinforcement arcs on {00.2}
509 and {10.0} PFs at 5° and 85° (identified by dashed orange rings in **Fig. 12 a**), respectively.
510 On the {10.0} PF, the orientation reinforcement is preferably done at 90° from the loading
511 direction in the sheet plane (TD).

512 In the second configuration considered (b), the compression twin mode $\{10.1\}\langle 10.2\rangle$
513 causes a crystal reorientation of 56° . Therefore, the resulting orientations of the twinned
514 basal plane (00.2) and twinned prismatic plane (10.0) to the sample surface are 56° and
515 34° , respectively (displayed by pink dashed line lattice projection in **Fig. 12 b**). These
516 crystallographic reorientations are highlighted by intensity reinforcement rings (dashed
517 pink rings in **Fig. 12 a**) that can be observed on {00.2} and {10.0} PFs at 56° and 34° ,
518 respectively.

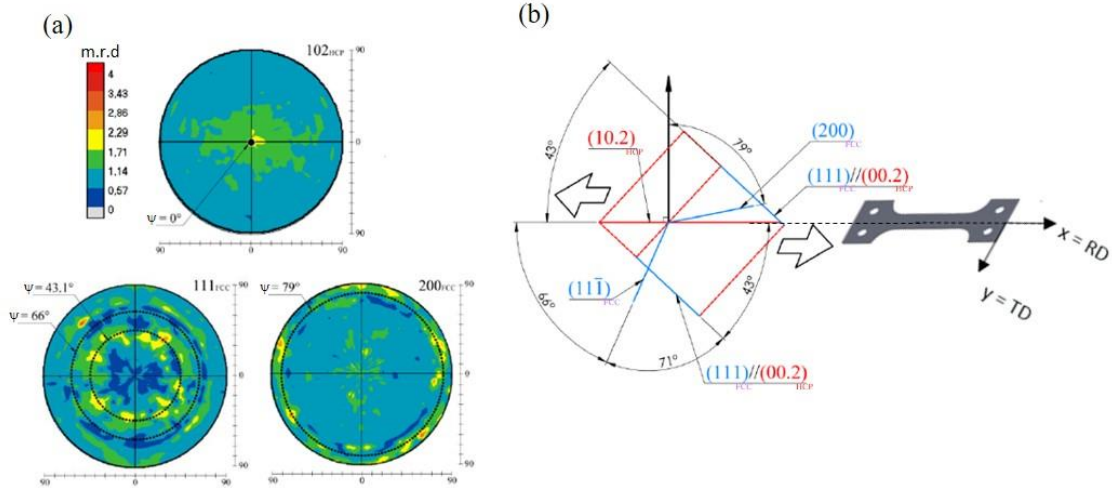


519

520 **Figure 12:** Identification of $\{10.2\}\langle 10.1 \rangle$ tensile twinning system, $\{10.1\}\langle 10.2 \rangle$
 521 compression twinning system and phase transformation on $\{00.2\}$ and $\{10.0\}$ PFs for the
 522 sample loaded up to 7.8 % strain (a). Schematic representation of reorientations caused
 523 by the two twin systems (b).

524

525 In the third configuration considered (c): the FCC \rightarrow HCP phase transformation induced
 526 by tensile straining can be observed on $\{10.2\}$, $\{00.2\}$, $\{111\}$ and $\{200\}$ PFs (dashed
 527 black circle in **Fig. 12 a** and **Fig. 13 a**). Because of the intermediate inclination of the
 528 HCP lattice, the (10.2) HCP plane is parallel to the sheet plane. Thus, the ND matches the
 529 central pole (at $\psi = 0^\circ$) observed on the $\{10.2\}$ PF. As described above, the FCC \rightarrow HCP
 530 phase transformation is multi-variant, and may occur on several $\{111\}$ FCC planes. For
 531 this configuration and considering the Shoji-Nishiyama's relationship, the habit plane
 532 $(111)//(00.2)$ is at an angle of 43.1° to the sample surface and the $(11\bar{1})$ one at an angle
 533 of 66° , as illustrated on $\{00.2\}_{HCP}$ and $\{111\}_{FCC}$ PFs (dashed black circle in **Fig. 12 a** and
 534 **Fig. 13 a**). Finally, the (200) FCC plane is oriented at 79° to the ND and depicted by an
 535 intensity reinforcement located at this ψ value on the $\{200\}_{FCC}$ PF.



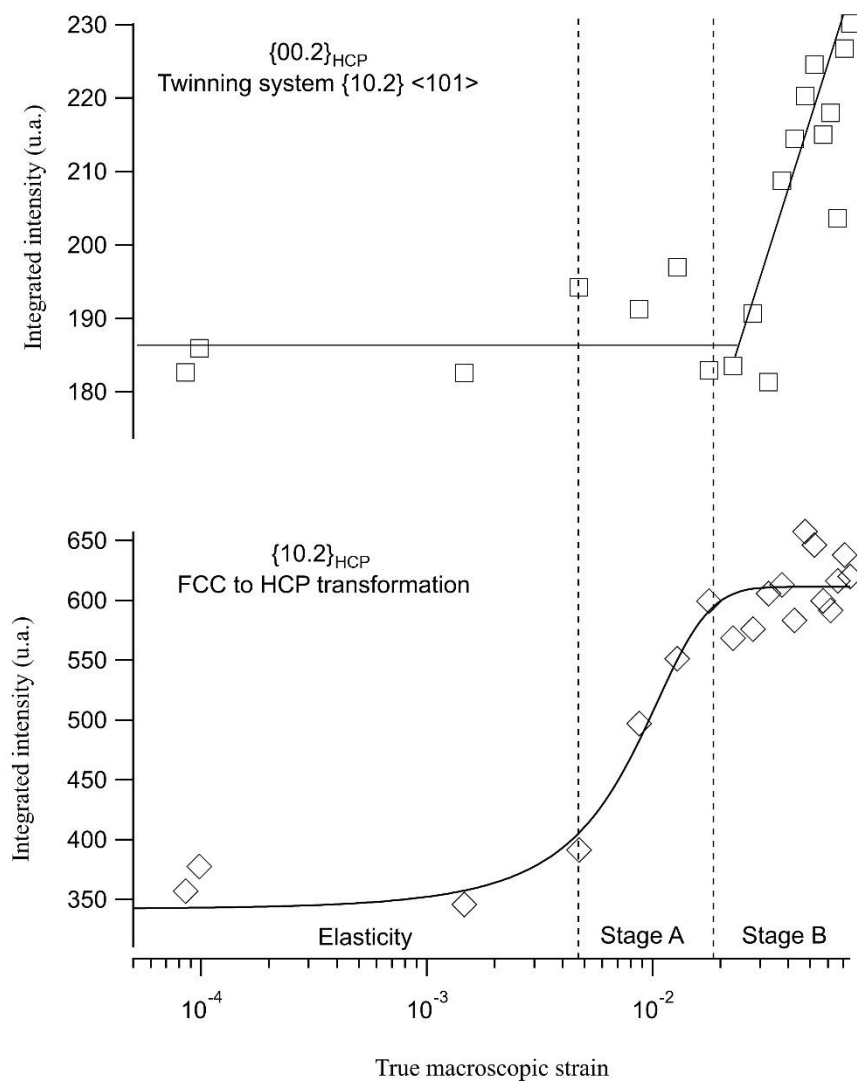
536

537 **Figure 13:** Identification of the phase transformation from $\{10.2\}_{\text{HCP}}$, $\{111\}_{\text{FCC}}$ and
 538 $\{200\}_{\text{FCC}}$ PFs for the sample loaded up to 7.8 % (a). Schematic representation of
 539 misorientations caused by the phase transformation (b).

540

541 Another way to analyze the evolution of the FCC \rightarrow HCP phase transformation with the
 542 mechanical loading as well as the **evolution** of the main tensile twin deformation mode
 543 ($\{10.2\}\langle 10.1 \rangle$) is to follow the integrated intensities of the peaks reflecting these two
 544 phenomena. **Fig. 14** shows the tracking of the integrated intensities of $\{00.2\}$ and $\{10.2\}$
 545 peaks during straining (for ψ respectively close to 5° and 0°) which correspond,
 546 respectively, to the activity of the twinning mode $\{10.2\}\langle 10.1 \rangle$ and the FCC \rightarrow HCP
 547 phase transformation. It can be seen that the integrated intensity of the peak $\{00.2\}$
 548 remains unchanged during straining until the beginning of stage B for which plasticity is
 549 governed by **twinning**. Thereafter, the integrated intensity of the $\{00.2\}$ reflection linearly
 550 increases with the macroscopic strain. The monitoring of the **integrated** intensity of the
 551 $\{10.2\}$ peak shows that the phase transformation, initiated by basal slip, starts at the
 552 beginning of the plasticity, in agreement to the results obtained for the FCC volume
 553 fraction evolution (see **Fig. 9**). Subsequently, the integrated intensity of the $\{10.2\}$ peak
 554 increases with macroscopic strain until the end of stage A. At this strain level, the

555 twinning mechanism is activated and becomes the main deformation mode, which causes
 556 a lattice reorientation and a possible stress relaxation. Therefore, the slope of the
 557 integrated intensity evolution of $\{10.2\}$ reflection tends towards 0, and remains
 558 unchanged with increasing macroscopic strain. Thus, at stage B, the evolution of the
 559 integrated intensity of the $\{10.2\}$ reflection seems to reflect a competition between the
 560 phase transformation and the twinning process.

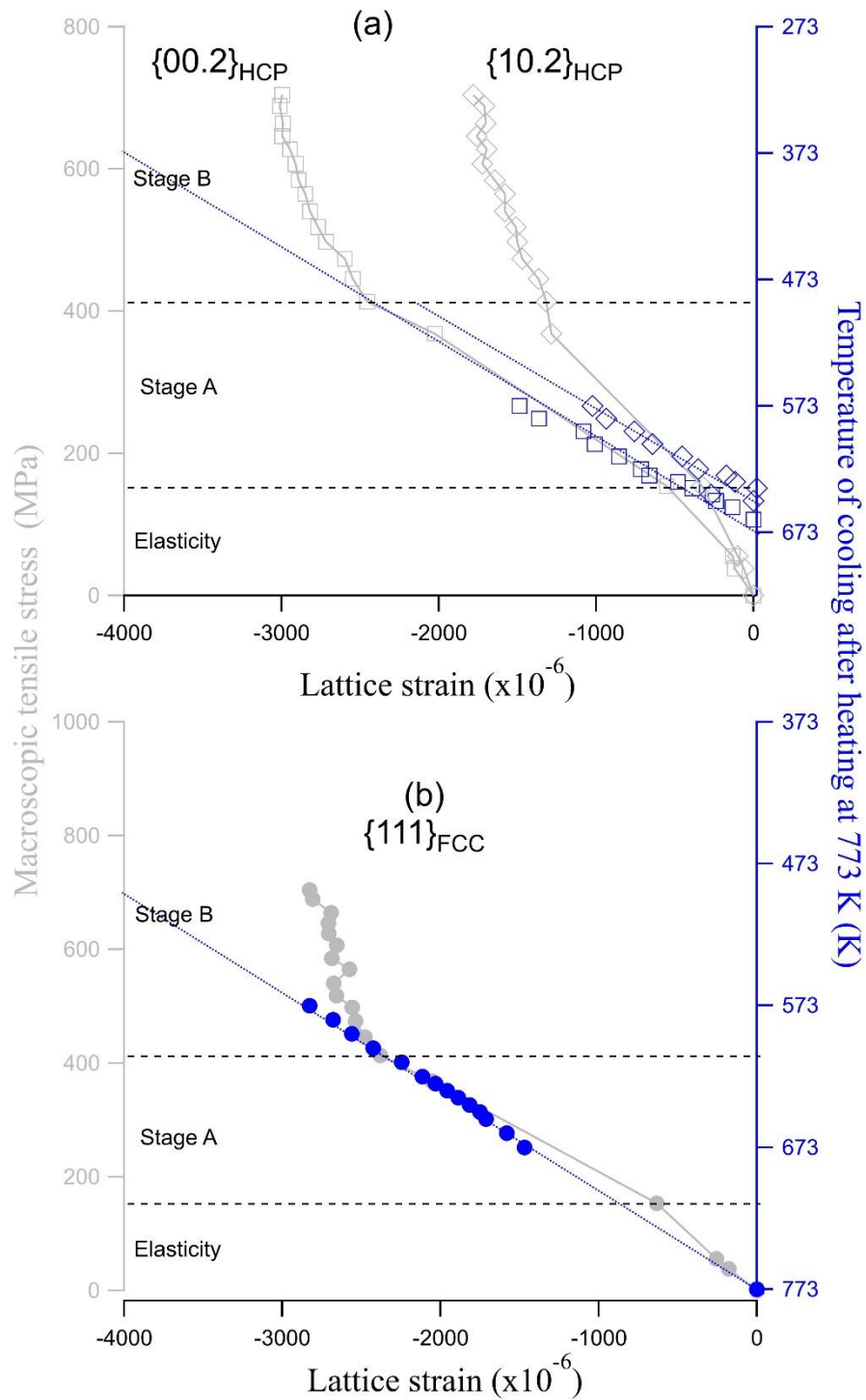


561

562 **Figure 14:** Evolution of the integrated peak intensity at $\psi = 0^\circ$ for the $\{10.2\}$ reflection
 563 and around $\psi = 5^\circ$ for the $\{00.2\}$ reflection during a tensile test along the rolling direction.

564

565 The monitoring of internal lattice strains (determined using the eq. (3)) of some $\{hkl\}$
566 plane families of HCP and FCC phases during tensile tests is illustrated on **Fig. 15**. In
567 order to compare these results with those obtained during the cooling of the thermal cycle
568 (subsection 3.1.2), the internal lattice strains related to the two loading types (thermal and
569 mechanical) are thus superimposed while adapting the temperature range of the thermal
570 loading to the FCC \rightarrow HCP phase transformation window so that it suits the stage A of
571 the tensile test, for which only the FCC \rightarrow HCP phase transformation is occurring. As
572 can be seen in **Fig. 15**, this means that the slope of the curves macroscopic stress vs.
573 lattice strains (in grey) during the tensile loading in stage A is similar to the slope of the
574 curves temperature vs. lattice strains (in blue) obtained during cooling, except for the case
575 of the $\{10.2\}$ reflection, which exhibits a higher slope in stage A. For reminder the $\{00.2\}$
576 basal slip is the only deformation mode in this stage. It comes along with a phase
577 transformation which occurs in a plane shared by the two FCC and HCP crystallographic
578 structures (i.e. the habit plane). From the beginning of stage B, a deviation from this
579 linearity appears, leading to a lower evolution of the internal lattice strains with the
580 macroscopic stress. The main deformation mode in stage B is twinning (mostly $\{10.2\}$
581 type) which induces reorientations of the crystal lattice. Thus, a stress relaxation can be
582 generated within twinned grains and causes a lattice strain decrease. In this stage a
583 competition between twinning and phase transformation can therefore be highlighted.
584 The comparison between the internal lattice strain values at the beginning of stage B
585 shows that the $\{10.2\}$ family plane deforms elastically less than the others before
586 twinning. This result is consistent with the fact that, in the configuration (10.2) plane
587 parallel to the sheet plane (c), the deformation can be accommodated by basal slip before
588 that plasticity is controlled by [twinning](#).



589

590 **Figure 15:** Example of lattice strains for $\{00.2\}_{\text{HCP}}$ and $\{10.2\}_{\text{HCP}}$ (a) and $\{111\}_{\text{FCC}}$ (b)
 591 reflections during a tensile test along the rolling direction (grey symbol) with those
 592 measured during a cooling stage after a heating at 773 K (blue symbol).

593

594

595 **4. Conclusions**

596 In the present work, new experimental results refresh and reinforce a scarce and dated to
597 1960's literature on phase transformations and strengthening mechanisms of
598 polycrystalline cobalt. The specific *in situ* temperature experiments have showed that the
599 FCC ↔ HCP phase transformation displays a temperature hysteresis between heating and
600 cooling coupled to a macroscopic dilatometric hysteresis. However, the analysis of elastic
601 lattice strains during the transformation does not exhibit this phenomenon.
602 Complementary XRD studies of the phase transformation have highlighted the influence
603 of the initial microstructure. In this work, a new and original *in situ* XRD study under
604 mechanical loading has been performed revealing that the martensitic transformation of
605 the initial FCC residual phase can be induced by the plasticity and coupled with the strain-
606 hardening mechanisms. FCC to HCP transformation is activated by basal slip during the
607 work-hardening stage A and continues during stage B with a competition with the twin
608 mode.

609

610 **References**

- 611 [1] G. Bouquet, B. Dubois: *Scr. Metall.*, 1978, vol. 12, pp. 1079–1081.
612 [2] A.E. Ray, S.R. Smith, J.D. Scofield: *J. Phase Equilibria*, 1991, vol. 12, pp. 644–
613 648.
614 [3] G. Fleurier, E. Hug, M. Martinez, P.-A. Dubos, C. Keller: *Philos. Mag. Lett.*, 2015,
615 vol. 95, pp. 122–130.
616 [4] H. Matsumoto: *J. Alloys Compd.*, 1995, vol. 223, pp. L1–L3.
617 [5] H. Matsumoto: *Phys. B Condens. Matter.*, 2003, vol. 334, pp. 112–117.
618 [6] C.R. Houska, B.L. Averbach, M. Cohen: *Acta Metall.*, 1960, vol. 8, pp. 81–87.
619 [7] C.C. Sanderson: PhD Thesis, University of British Columbia, 1972.
620 [8] V.M. Marx, C. Kirchlechner, B. Breitbach, M.J. Cordill, D.M. Töbrens, T. Waitz,
621 G. Dehm: *Acta Mater.*, 2016, vol. 121, pp. 227–233.
622 [9] M. Martinez, G. Fleurier, F. Chmelík, M. Knappek, B. Viguier, E. Hug: *Mater.*
623 *Charact.*, 2017, vol. 134, pp. 76–83.
624 [10] A. Seeger, H. Kronmüller, S. Mader, H. Träuble: *Philos. Mag.*, 1960, vol. 6, pp.
625 639–655.
626 [11] G. Fleurier, M. Martinez, P.A. Dubos, E. Hug: *Mater. Sci. Forum.*, 2017, vol. 879,
627 pp. 560–565.
628 [12] J.W. Christian, W. Hume-Rothery: *Proc. R. Soc. Lond. Ser. Math. Phys. Sci.*,
629 1951, vol. 206, pp. 51–64.
630 [13] H.T. Hesemann, P. Müllner, E. Arzt: *Scr. Mater.*, 2001, vol. 44, pp. 25–30.
631 [14] H.T. Hesemann, P. Müllner, O. Kraft, D. Nowak, S.P. Baker, K. Finkelstein, E.
632 Arzt: *Scr. Mater.*, 2003, vol. 48, pp. 1129–1133.
633 [15] H.-R. Wenk, S. Matthies, J. Donovan, D. Chateigner: *J. Appl. Crystallogr.*, 1998,
634 vol. 31, pp. 262–269.
635 [16] N. Bruzy: PhD Thesis, Ecole Centrale de Nantes, 2018.
636 [17] N. Bruzy, M. Coret, B. Huneau, G. Kermouche, M. Mondon, E. Bertrand, L.
637 Stainier: *Exp. Mech.*, 2019, vol. 59, pp. 1145–1157.
638 [18] W.A. Rachinger: *J. Sci. Instrum.*, 1948, vol. 25, pp. 254–255.
639 [19] M.J. Buerger: *Proc. Natl. Acad. Sci.*, 1940, vol. 26, pp. 637–642.
640 [20] J.T. Bonarski, M. Wróbel, K. Pawlik: *Mater. Sci. Technol.*, 2000, vol. 16, pp. 657–
641 662.
642 [21] W. Betteridge: *Prog. Mater. Sci.*, 1980, vol. 24, pp. 51–142.
643 [22] K. Lonsdale, C. H. MacGillavry, G D. Rieck: *International Tables for X-Ray*
644 *Crystallography*, Kynoch Press, 1962, vol 3.
645 [23] R. Bauer, E.A. Jaegle, W. Baumann, E.J. Mittemeijer: *Philos. Mag.*, 2010, vol. 91,
646 pp. 437–457.
647 [24] D. Gloaguen, B. Girault, B. Courant, P.-A. Dubos, M.-J. Moya, F. Edy, J. Rebelo
648 Kornmeier: *Metall. Mater. Trans. A.*, 2020, vol. 51, pp. 951–961.
649 [25] H. Bibring, F. Sebilliau: *Rev. Métallurgie.*, 1955, vol. 52, pp. 569–578.
650 [26] G.W. Greenwood, R.H. Johnson: *Proc. R. Soc. Lond. Ser. Math. Phys. Sci.*, 1965,
651 vol. 283, pp. 403–422.
652 [27] G. Fleurier: PhD Thesis, Université de Caen, 2016.
653 [28] A. Zhou: PhD Thesis, Drexel University, 2008.
654 [29] A.G. Zhou, D. Brown, S. Vogel, O. Yeheskel, M.W. Barsoum: *Mater. Sci. Eng.*
655 *A.*, 2010, vol. 527, pp. 4664–4673.
656 [30] Y.N. Wang, J.C. Huang: *Mater. Chem. Phys.*, 2003, vol. 81, pp. 11–26.

- 657 [31] J.W. Christian, S. Mahajan: Prog. Mater. Sci., 1995, vol. 39, pp. 1–157.
658 [32] M.H. Yoo: Metall. Trans. A., 1981, vol. 12, pp. 409–418.
659 [33] M. Martinez, E. Hug: Materialia, 2019, vol. 7, pp. 100420.
660 [34] S. Vaidya, S. Mahajan, C.M. Preece: Metall. Trans. A., 1980, vol. 11, pp. 1139–
661 1150.
662 [35] Z. Nishiyama: Martensitic Transformation - 1st Edition, Academic Press, 1978.
663 [36] F. Sebilliau, H. Bibring: Inst. Met. Monogr., 1956, vol. 18, pp. 209–217.
664

665 **Figures captions:**

666

667 **Graphical abstract:** Evolution of metastable cobalt FCC volume proportion during
668 thermal cycle and mechanical loadings.

669

670 **Figure 1:** EBSD Image Quality (IQ) map and phase cartography of as-received cobalt
671 microstructure.

672

673 **Figure 2:** Diffraction patterns for $\{111\}_{\text{FCC}}$ and $\{00.2\}_{\text{HCP}}$ reflections during heating and
674 cooling.

675

676 **Figure 3:** Volume fraction of FCC phase during heating (red circle) and cooling (blue
677 square) of cobalt calculated from XRD data. Error bars are the standard deviation on the
678 8 couples of family planes.

679

680 **Figure 4:** Mechanical state during thermal cycle considering the different tracked plane
681 families. (a) Lattice strain evolution during heating (red) and cooling (blue). (b)
682 Thermal expansion coefficients during heating (red open circle) and cooling (blue open
683 circle) obtained from XRD results. (c) Measured residual lattice strains after (black
684 solid circle) the thermal cycle.

685

686 **Figure 5:** Dilatometric curves according to ε_{xx} , ε_{yy} and γ_{xy} during the thermal cycle. (x
687 corresponds for this experiment to the rolling direction).

688

689 **Figure 6:** Influence of annealing conditions (temperature for a time of 1h (a) and time for
690 a temperature of 1373°K (b)) on grain size and retained FCC phase proportion evolution.

691

692 **Figure 7:** Thermal loading paths in DSC performed for as-received (a), 573 K (b),
693 673 K (c) and 773 K (d) annealed samples with corresponding austenitic (red) and
694 martensitic (blue) transformation peak tracking.

695

696 **Figure 8:** Temperatures of HCP \rightarrow FCC and FCC \rightarrow HCP transformations as a function
697 of the number of applied DSC cycles (up to 30 cycles) of as-received sample superposed
698 with the result of 573 K, 673 K and 773 K annealed samples.

699

700 **Figure 9:** FCC \rightarrow HCP transformation evolution as macroscopic strain increases.
701 Relationship between FCC phase proportion (red open triangle) and the deformation
702 stages illustrated by work-hardening (black open square). Monitoring of the phase
703 transformation anisotropy for various (ϕ , ψ) orientations (maps) during tensile straining
704 with the corresponding average values (red solid circle).

705

706 **Figure 10:** $\{10.0\}_{\text{HCP}}$, $\{00.2\}_{\text{HCP}}$, $\{10.1\}_{\text{HCP}}$, $\{10.2\}_{\text{HCP}}$, $\{111\}_{\text{FCC}}$ and $\{200\}_{\text{FCC}}$
707 recalculated PFs of the as-received sample and of a sample strained at 7.8 % along RD.

708

709 **Figure 11:** Schematic representation of the orientation relationship between the FCC
710 structure (in blue) and the HCP structure (in red) once shear has been achieved along
711 the $[11\bar{2}]$ FCC direction.
712

713 **Figure 12:** Identification of $\{10.2\}\langle 10.1\rangle$ tensile twinning system, $\{10.1\}\langle 10.2\rangle$
714 compression twinning system and phase transformation on $\{00.2\}$ and $\{10.0\}$ PFs for
715 the sample loaded up to 7.8 % strain (a). Schematic representation of reorientations
716 caused by the two twin systems (b).
717

718 **Figure 13:** Identification of the phase transformation from $\{10.2\}_{\text{HCP}}$, $\{111\}_{\text{FCC}}$ and
719 $\{200\}_{\text{FCC}}$ PFs for the sample loaded up to 7.8 % (a). Schematic representation of
720 misorientations caused by the phase transformation (b).
721

722 **Figure 14:** Evolution of the integrated peak intensity at $\psi = 0^\circ$ for the $\{10.2\}$ reflection
723 and around $\psi = 5^\circ$ for the $\{00.2\}$ reflection during a tensile test along the rolling direction.
724

725 **Figure 15:** Example of lattice strains for $\{00.2\}_{\text{HCP}}$ and $\{10.2\}_{\text{HCP}}$ (a) and $\{111\}_{\text{FCC}}$ (b)
726 reflections during a tensile test along the rolling direction (grey symbol) with those
727 measured during a cooling stage after a heating at 773 K (blue symbol).
728
729

730 **Tables captions:**

731

732 **Table 1:** XRD reflections tracked for each experiment and the plane family couples used
733 for the phase volume fraction calculations.

734

735 **Table 2:** Applied temperatures for *in situ* XRD experiments during thermal cycle
736 (heating rate 0.5 K/s between each temperature step – 1h acquisition duration for each
737 temperature).

738

739 **Table 3:** {00.2} and {10.0} PF reorientations peculiar to twinning systems and phase
740 transformation according to the 3 studied configurations.